Functional Materials Letters
Vol. 12, No. 1 (2019) 1850089 (5 pages)

DOI: 10.1142/S1793604718500893

Solvent-mediated crystalline phases of Ni_xS_y anchored on rGO sheets as electrocatalysts for hydrogen evolution application

Hou Lin Yu*, Wenliang Shi*, Shuaishuai Li*, Junma Zhang*, Xiaobo Zhang*,
Huaping Wu†, Tingyu Zhao*,¶ and Aiping Liu*,‡,§,||
*Center for Optoelectronics Materials and Devices
Zhejiang Sci-Tech University, Hangzhou 310018, P. R. China
†Laboratory of E&M (Zhejiang University of Technology)
Ministry of Education & Zhejiang Province, Hangzhou 310014, P. R. China
‡State Key Laboratory of Structural Analysis for Industrial Equipment
Dalian University of Technology, Dalian 116024, P. R. China
§State Key Laboratory of Digital Manufacturing Equipment and Technology
Huazhong University of Science and Technology
Wuhan 430074, P. R. China
¶zhaotingyu@zstu.edu.cn
||liuaiping1979@gmail.com

Received 12 June 2018; Accepted 10 July 2018; Published 14 August 2018

A facile, one-pot solvent-mediated hydrothermal process was adopted to prepare nickel sulfide nanoparticles decorated on reduced graphene oxide (Ni_xS_y/rGO) as electrocatalysts for hydrogen evolution reaction (HER). The designed solvent (ethylene glycol and deionized water) played a decisive role in controlling both crystalline phase and morphology of Ni_xS_y/rGO composites, leading to pure α-NiS nanoparticles uniformly distributed on rGO sheets under suitable volume ratio of ethylene glycol and deionized water (2:1). The optimized α-NiS/rGO showed prominent HER catalytic performance with a rather small Tafel slope of 93 mV/decade and prominent current density of 10 mA/cm^2 at the overpotential of 177 mV in alkaline environments when compared to pristine α-NiS and NiS_2/rGO catalysts. The excellent catalytic performance and long-term durability even after 8000 cycles confirmed the potential of α-NiS/rGO composites as efficient electrocatalysts for HER in the alkaline media.

Keywords: Nickel sulfide; crystalline phase; hydrogen evolution reaction; solvent assistance; alkaline condition.

Hydrogen energy has been considered as the most promising alternative energy to the traditional hydrocarbon fuels due to its clean, renewable and sustainable properties.[1,2] Electrocatalytic hydrogen evolution reaction (HER) has achieved encouraging progress with the designing of novel and effective HER catalysts which have dramatically reduced the overpotential of hydrogen evolution in recent years.[3–5] Transition metal dichalcogenides and corresponding composites, such as MoS_2,[2,5–8] WS_2,[9] MoS_xSe_{2-x} alloys,[10] and so on have been demonstrated as efficient HER catalysts in acid conditions. Recently, nickel sulfides (Ni_xS_y), such as NiS,[11] NiS_2,[12] and Ni_3S_2[3] have presented outstanding HER performances in alkaline media due to their adjustable active surface area and intrinsic conductivity. Moreover, the HER performance of Ni_xS_y-based catalysts greatly depend on the crystalline phases of materials.[4,11,13] For instance, Chung *et al.* experimentally found the superior HER performance of NiS over that of Ni_3S_2 in alkaline media.[13] Jiang *et al.* successfully synthesized Ni_xS_y with various phases including NiS, NiS_2 and Ni_3S_2 by adjusting the amounts of S source, confirming the highest HER activity of Ni_3S_2 in alkaline media.[11] However, these synthesis procedures are either complicated or energy-guzzling. Thus, it is reasonable to design a facile synthesis method of Ni_xS_y with controllable phase structures for further improvement of HER performance.

In this paper, we demonstrate a one-step solvent-assisted hydrothermal process to fabricate Ni_xS_y nanoparticles decorated on reduced graphene oxide (rGO) sheets. The volume

---

¶,||Corresponding authors.

ratio of ethylene glycol (EG) and deionized water (D.I. water) in the mixed solvent plays critical roles in controlling the crystalline phase and morphology of Ni_xS_y, resulting in uniform size distribution of α-NiS nanoparticles on rGO surface at optimized volume ratio of EG and D.I. water. The well-designed α-NiS/rGO composites with improved conductivity show superior HER catalytic activity (than pristine α-NiS and NiS_2/rGO) with a small onset overpotential of only 80 mV, small Tafel slope as low as 93 mV/decade, extremely high exchange current density of 0.141 mA/cm^2 and excellent stability even after 8000 cyclic voltammetry tests in alkaline condition.

GO was synthesized through the improved Hummer's method.[14] Typically, a mixed solvent of H_2SO_4 and H_3PO_4 (volume ratio of 9:1) was added to the mixture of graphite and $KMnO_4$ and preheated at 40°C for 1 h. After that, the temperature was increased to 50°C and kept stirring for about 12 h. Then, the reaction was cooled naturally to room temperature and terminated by adding ice water with 30% H_2O_2. The obtained products were washed and exfoliated by centrifugation to obtain GO suspension (9 mg/mL). For Ni_xS_y/rGO composites preparation, 15 mL of mixed solvent was added to the mixture of GO, $NiCl_2.6H_2O$ and thiourea under sonication. Then, the suspension was transferred to a 25 mL Teflon-lined autoclave and heated in an oven at 200°C for 18 h. The black products were collected by centrifugation and vacuum-dried at 60°C overnight. Changing the amount of EG in the mixed solvent (0, 5, 7.5, 10 ml and 15 mL), different Ni_xS_y/rGO composites were obtained and named as Ni_xS_y/rGO-0, Ni_xS_y/rGO-5, Ni_xS_y/rGO-7.5, Ni_xS_y/rGO-10, and Ni_xS_y/rGO-15, respectively. Pristine Ni_xS_y as the reference was synthesized with the same process except GO addition (10 mL EG was used). In order to investigate the synergistic effect between Ni_xS_y and rGO, pure rGO was prepared except for the adding of $NiCl_2.6H_2O$ and thiourea precursors. The mechanical mixture of pristine Ni_xS_y and rGO was prepared by mechanical ultrasonic treatment for 1 h.

The morphologies of Ni_xS_y/rGO composites were observed by a Field Emission Scanning Electron Microscope (FESEM, vltra 55). Transmission Electron Microscopy (TEM) images were collected on a Hitachi H-7650 at 200 kV. X-ray diffraction (XRD) measurements were performed on an X-ray diffractometer (Bruker AXS D8) using the Cu Ka radiation ($\lambda = 0.15418$ nm). Raman spectra were recorded on a Thermo Fisher DXR Raman spectrometer with a He-Ne laser ($\lambda = 632.8$ nm). X-ray photoelectron spectroscopy (XPS) was collected by an X-ray photoemission spectrometer (KRATOS AXIS ULTRA-DLD). The Brunauer–Emmett–Teller (BET) surface area and porosity were estimated by analyzing the adsorption–desorption isotherms (Micromeritics ASAP2020, United States). The thermal gravimetric analysis (TGA) was conducted on a TA Q500 Instrument under flowing air at a heating rate of 10°C min^{-1}. For electrode preparation, 5 mg catalysts and 80 μL nafion solution (5 wt.%) were dispersed in 1 mL water-ethanol solution (volume ratio of 3:1) and sonicated for about 0.5 h to obtain a homogeneous ink. Then 5 μL of black slurry was drop-casted onto the glass carbon electrode (loading ca. 0.354 mg.cm^{-2}) and dried at room temperature. The electrochemical measurements were carried out in a three-electrode setup on a CHI 660D workstation (Shanghai Chenhua Instrument Co., China). A saturated calomel electrode (SCE) and a Pt wire were used as the reference electrode and counter electrode, respectively. Linear sweep voltammogram scan (5 mV/s) was conducted in a 1 M KOH solution purged in pure N_2. Durability test was performed through cyclic voltammetry method from 0.1 V to -0.4 V at 100 mV/s for 8000 cycles. The electrochemical impedance spectrum (EIS) measurement was carried out at an overpotential of 100 mV from 10^5 Hz to 0.1 Hz at 5 mV. All potentials were calibrated to reversible hydrogen electrode (RHE) according to previous report.[13] All electrochemical data were presented with iR compensation.

Figure 1 shows the morphologies of pristine Ni_xS_y and Ni_xS_y/rGO composites. Pristine Ni_xS_y microspheres (volume ratio of EG and D.I. water is 2:1) aggregate seriously with sizes changing from submicrometers to several micrometers (Fig. 1(a)). For Ni_xS_y/rGO composites, the morphologies drastically change with increasing EG volume in the mixed

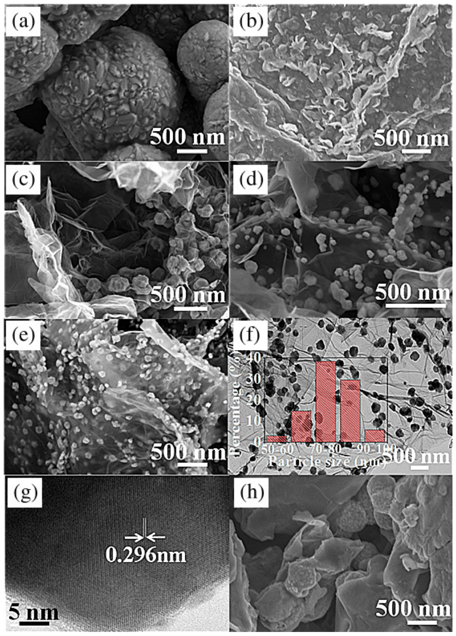

Fig. 1. Scanning electron microscopy images of (a) Ni_xS_y, (b) Ni_xS_y/rGO-0, (c) Ni_xS_y/rGO-5, (d) Ni_xS_y/rGO-7.5, (e) Ni_xS_y/rGO-10 and (h) Ni_xS_y/rGO-15. (f) TEM image and (g) corresponding HRTEM image of Ni_xS_y/rGO-10 composites. The inset is size distribution chart of Ni_xS_y/rGO-10.

solvent. The Ni_xS_y nanosheets are stacked together on rGO surfaces when pure D.I. water is used (Fig. 1(b) for Ni_xS_y/rGO-0). When 5 mL of EG is added into the mixed solvent, aggregated Ni_xS_y nanoparticles about 100 nm could be observed (Fig. 1(c) for Ni_xS_y/rGO-5). With the amount of EG further increasing to 7.5 mL, the average size of Ni_xS_y nanoparticles decreases to 70 nm with part aggregation (Fig. 1(d)). For the Ni_xS_y/rGO-10, the Ni_xS_y nanoparticles with an average size of 76 nm (inset in Fig. 1(f)) are homogeneously distributed on rGO surface (Figs. 1(e) and 1(f)). The HRTEM image (Fig. 1(g)) reveals that this crystal plane distance of Ni_xS_y for Ni_xS_y/rGO-10 is 0.296 nm, which is consistent with the previous report about α-NiS.[15,16] Finally, when the D.I. water is totally replaced by EG (Ni_xS_y/rGO-15), the aggregated Ni_xS_y microspheres form and obviously separate with rGO (Fig. 1(h)). Therefore, an appropriate solvent ratio is important for controllable growth of Ni_xS_y nanoparticles with narrow size distribution on rGO surface. Additionally, the abundant surfaces of rGO provide sufficient nucleating points to prevent Ni_xS_y nanoparticles from agglomeration.[17] Figure 2(a) shows XRD curves of different Ni_xS_y/rGO composites. Pure Ni_xS_y and Ni_xS_y/rGO-10 show four main peaks located at 30.2°, 34.7°, 45.9° and 53.6°, which can be assigned to (100), (101), (102) and (110) crystal planes of α-NiS (JCPDS No. 02-1280).[16,18] This is in accordance with the observation in Fig. 1(g) because the distance of (100) crystal plane of α-NiS is about 0.296 nm. The Ni_xS_y/rGO-7.5 shows different diffraction peaks at 31.6°, 35.4°, 38.9°, 45.3° and 53.5°, which could be assigned to the (200), (210), (211), (220) and (311) crystal planes of NiS_2 (JCPDS No. 11-0099).[11,12] For Ni_xS_y/rGO-0, Ni_xS_y/rGO-5, and Ni_xS_y/rGO-15, the XRD results display the mixed phases of α-NiS and NiS_2. Our results indicate that the crystalline structures of Ni_xS_y anchored on rGO sheets can be effectively controlled only by adjusting the constituent of a mixed solvent during the hydrothermal process. The broad diffraction peak at 24.1° indicates the stacking process of graphite (002) crystal planes during the hydrothermal process.[7] Figure 2(b) exhibits the Raman shifts of GO, Ni_xS_y/rGO-7.5 (NiS_2/rGO) and Ni_xS_y/rGO-10 (α-NiS/rGO) composites. Two characteristic peaks of rGO indicated as D band and G band could be observed at 1335 cm^{-1} and 1585 cm^{-1}, respectively, which represent the defect and disordered carbon (D-band) and vibrations of ordered sp^2-hybridized carbon atoms (G-band), respectively.[19] The relative intensity ratio of I_D/I_G is about 1.13 and 1.23 for NiS_2/rGO and α-NiS/rGO, respectively, compared to the 0.98 for GO, indicating the decreased average size of sp^2 domains and successful reduction from GO to rGO during hydrothermal treatment.[2,5] However, the vibration modes related to α-NiS and NiS_2 cannot be observed due to the effect of quantum confinement on vibrational modes in Ni_xS_y nanoparticles.[20] The XPS spectra illustrate the chemical states of pure Ni_xS_y and Ni_xS_y/rGO with binding energies of Ni $2p_{3/2}$ and Ni $2p_{1/2}$ at about 853.1 eV and 870.8 eV, respectively (Fig. 2(c)). The peaks located at 859.7 eV could be assigned to the satellite peak of Ni $2p_{3/2}$. Moreover, the peaks located at 855.3 eV could be attributed to the trace of oxidation state of Ni^{2+},[21] which might be responsible for the HER process in alkaline condition. Note that the binding energies of Ni $2p_{3/2}$ peaks of α-NiS and NiS_2 are essentially similar due to the exhibition of metal character (Ni^{2+}) but not the sulfur atoms.[11] For the Ni_xS_y/rGO system, a stronger interaction with rGO and Ni_xS_y might be presented due to their coelectron cloud overlapping, resulting in slightly higher binding energies of Ni $2p_{1/2}$ in the Ni_xS_y/rGO system when compared to the Ni_xS_y (Fig. 2(c)).[21] This is helpful for the electron transfer from rGO to Ni_xS_y in the HER process. The characteristic peaks located at 161.3 eV and 162.9 eV can be assigned to S $2p_{3/2}$ and S $2p_{1/2}$, respectively (Fig. 2(d)), which stems from the bridging S_2^{2-} ligand or the apical S^{2-} one.[7,22] The N_2 adsorption/desorption isotherm in Fig. 3 shows a type IV curve with a hysteresis loop, suggesting the presence of mesopores, as shown in the pore size distribution (inset in Fig. 3). The BET surface areas are 22.9 m^2/g and 19.8 m^2/g for Ni_xS_y/rGO-10 (α-NiS/rGO) and Ni_xS_y/rGO-7.5 (NiS_2/rGO), respectively, demonstrating α-NiS/rGO might have multiple pore structures.

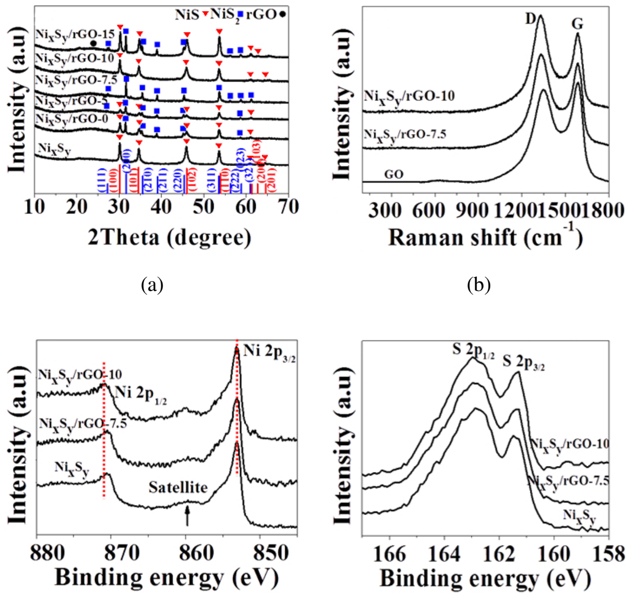

(a) (b)

(c) (d)

Fig. 2. (a) X-ray diffraction patterns of pristine Ni_xS_y and various Ni_xS_y/rGO composites, (b) Raman spectra of GO, Ni_xS_y/rGO-7.5 and Ni_xS_y/rGO-10. X-ray photoelectron spectra of (c) Ni 2p and (d) S 2p for pristine Ni_xS_y and various Ni_xS_y/rGO composites.

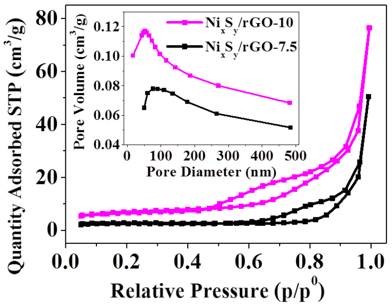

Fig. 3. N_2 absorption–desorption curves for Ni_xS_y/rGO-7.5 and Ni_xS_y/rGO-10. Inset shows the pore size distribution.

In order to reveal the influence of morphology and phase structure on HER activity of Ni_xS_y/rGO composites, electrochemical measurements were carried out in the alkaline environments. Figure 4(a) shows the polarization curves of various catalysts. The pristine Ni_xS_y (α-NiS) shows inferior catalytic ability for HER with rather larger onset overpotential of 182 mV (Table S1 in the supporting information), while the α-NiS/rGO composites exhibit excellent activity for HER with a small onset overpotential of only 80 mV. Moreover, it needs about 177 mV to reach 10 mA/cm^2 compared with 317, 229, 200, 210 and 271 mV for pristine α-NiS, Ni_xS_y/rGO-0, Ni_xS_y/rGO-5, NiS_2/rGO and Ni_xS_y/rGO-15, respectively. Though the morphology of NiS_2/rGO composites is similar to that of α-NiS/rGO, the HER performance of the latter is superior (Table S1). This could be assigned to the fact that the designed α-NiS/rGO have preferable HER activity than NiS_2/rGO in alkaline media, which is in good agreement with the previous report.[13] The Tafel curves are further obtained and the α-NiS/rGO composites exhibit the smallest Tafel slopes (Fig. 4(b) and Table S1), validating the preeminent HER activities. Such excellent HER performance for α-NiS/rGO could be rationalized as follows: (1) the designed volume ratio of the mixed solvent (2:1) is favorable to both adjust the morphology of the composites with good dispersion and control the crystalline phase of Ni_xS_y; (2) GO provides enough negatively charged active sites to effectively adsorb positively charged nickel ions,[6,23] resulting in uniformly dispersed α-NiS nanoparticles on rGO surface; (3) intimate contact between α-NiS nanoparticles and rGO improves not only the catalyst conductivity but also the stability due to the synergistic effect between α-NiS and rGO through the hydrothermal process.[24] This improved conductivity can be confirmed from the EIS result. The series resistance at high frequency are 6.8, 6.5, 6.2 and 6.0 Ω for pure α-NiS, mixture of α-NiS and rGO, NiS_2/rGO and α-NiS/rGO, respectively (Fig. 4(c)), indicating the excellent conductivity of the system. The semicircle of Nyquist plots related to charge transfer resistance (R_{ct}) for α-NiS/rGO is smallest, indicating a faster charge transfer process due to the enhanced conductivity of composites.[8] Additionally, the α-NiS/rGO composites present only a little decrease in the current density even after 1000 continuous cycles (Fig. 5(a)). The morphology of α-NiS/rGO composites almost remains unchanged, as shown in Fig. 5(b). While the mechanical mixture (with the same mass ratio to α-NiS/rGO obtained from

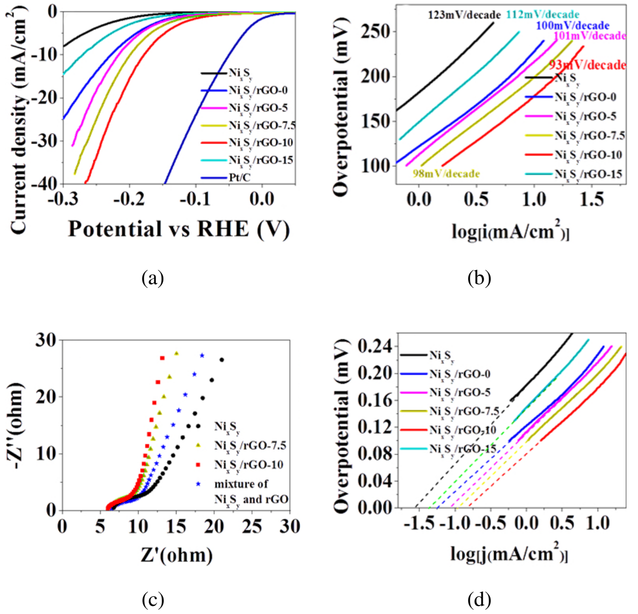

(a) (b)

(c) (d)

Fig. 4. (a) Polarization curves and (b) corresponding Tafel plots for different catalysts. (c) Nyquist plots of Ni_xS_y and Ni_xS_y/rGO catalysts, respectively. (d) Exchange current densities of various catalysts by using the extrapolation method.

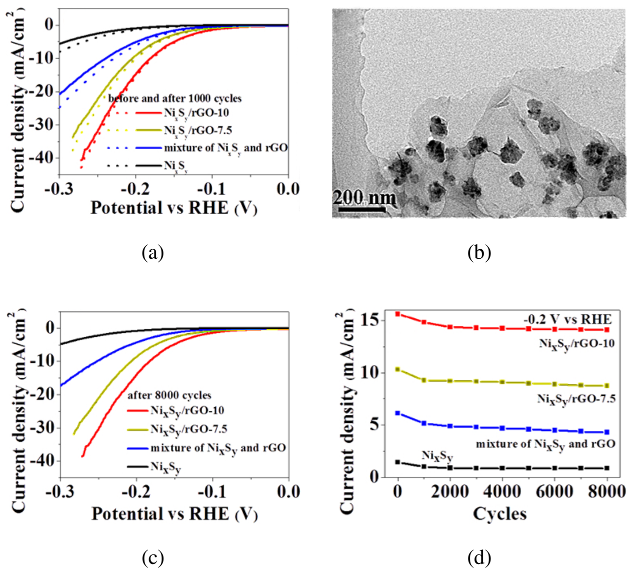

(a) (b)

(c) (d)

Fig. 5. (a) Durability test for different composites after 1000 cycles from −0.1 V−−0.4 V at 100 mV/s. (b) TEM image of the Ni_xS_y/rGO-10 composite after 1000 continuous cycles. (c) Durability test for different composites after 8000 cycles from −0.1 V−−0.4 V at 100 mV/s. (d) Change of HER cathodic current density at −0.2 V with respect to the cycle number.

TGA results) shows a 16.4% loss in the current density after 1000 cycles (Fig. 5(a)), indicating the inferior HER performance compared to the *in-situ* synthesized α-NiS/rGO. When the continuous potential scanning rises up to 8000 cycles (Fig. 5(c)), the cathodic current density of α-NiS/rGO at -0.2 V exhibits retention of $> 90\%$ (Fig. 5(d)), attesting to its excellent electrochemical durability. Additionally, the exchange current density is another critical criterion to evaluate the HER performance of composites.[25] The α-NiS/rGO shows the largest value of 0.141 mA/cm^2 (Fig. 4(d) and Table S1), which is superior than recently reported three-dimensionally ordered Ni[26] and porous MoC_x nano-octahedrons[27] (Table S2), indicating the excellent HER catalytic properties of α-NiS/rGO.

In summary, an efficient Ni_xS_y/rGO composite with well-controllable Ni_xS_y crystalline structure for hydrogen evolution application in the alkaline media has been successfully synthesized through a simple one-pot hydrothermal method. The volume ratio of the mixed solvent is proved to play key roles, not only in controlling morphology but also in crystalline phase adjustment of Ni_xS_y nanoparticles. Such α-NiS/rGO composites prepared at optimized volume ratio of mixed solvent present superior HER activity in alkaline media with a small onset overpotential of only 80 mV, high exchange current densities of 0.141 mA/cm^2, as well as outstanding cycling stability even after 8000 continuous cycles. The remarkable enhancement of HER activity could be attributed to the significantly improved conductivity, the formation of α-NiS nanoparticles with good dispersion and sufficiently exposed active sites on the surface of rGO, and synergistic effect between α-NiS and rGO. This may provide a potential way to design metal sulfides/rGO composites as a HER catalyst used in alkaline conditions.

Acknowledgements

This work was supported by the National Natural Science Foundation of China (No. 51572242), the Zhejiang Provincial Natural Science Foundation of China (No. LY16E020011), the 521 Talent Project of Zhejiang Sci-Tech University, the Program for Innovative Research Team of Zhejiang Sci-Tech University (No. 15010039-Y), the Opening Fund of State Key Laboratory of Structural Analysis for Industrial Equipment of Dalian University of Technology (No. GZ1704) and the Opening Fund of State Key Laboratory of Digital Manufacturing Equipment and Technology of Huazhong University of Science and Technology (No. DMETKF201817).

References

1. J. S. Luo *et al.*, *Science* **345**, 1593 (2014).
2. L. Zhao *et al.*, *Carbon* **116**, 223 (2017).
3. L. L. Feng *et al.*, *J. Am. Chem. Soc.* **137**, 14023 (2015).
4. X. Long *et al.*, *J. Am. Chem. Soc.* **137**, 11900 (2015).
5. A. P. Liu *et al.*, *ACS Appl. Mater. Interfaces* **8**, 25210 (2016).
6. Y. G. Li *et al.*, *J. Am. Chem. Soc.* **133**, 7296 (2011).
7. X. L. Zheng *et al.*, *Chem. Mater.* **26**, 2344 (2014).
8. J. M. Zhang *et al.*, *Electrochim. Acta* **182**, 652 (2015).
9. L. Cheng *et al.*, *Angew. Chem. Int. Ed.* **53**, 7860 (2014).
10. Q. F. Gong *et al.*, *ACS Catal.* **5**, 2213 (2015).
11. N. Jiang *et al.*, *Catal. Sci. Technol.* **6**, 1077 (2016).
12. C. Tang *et al.*, *Electrochim. Acta* **153**, 508 (2015).
13. D. Y. Chung *et al.*, *Nanoscale* **7**, 5157 (2015).
14. D. C. Marcano *et al.*, *ACS Nano* **4**, 4806 (2010).
15. L. Tian *et al.*, *Cryst. Growth Des.* **9**, 352 (2009).
16. X. Y. Yu *et al.*, *Angew. Chem. Int. Ed.* **54**, 5331 (2015).
17. X. Zhao *et al.*, *J. Mater. Chem. A* **5**, 7394 (2017).
18. H. Geng *et al.*, *J. Mater. Chem. A* **2**, 15152 (2014).
19. X. H. Wang *et al.*, *Biosens. Bioelectron.* **105**, 22 (2018).
20. A. Singh *et al.*, *J. Mater. Chem. A* **2**, 16723 (2014).
21. C. Kong *et al.*, *ACS Catal.* **4**, 2763 (2014).
22. Z. H. Deng *et al.*, *Chem. Commun.* **51**, 1893 (2015).
23. Z. C. Xing *et al.*, *Electrochem. Commun.* **32**, 9 (2013).
24. J. Q. Tian *et al.*, *J. Am. Chem. Soc.* **136**, 7587 (2014).
25. A. B. Laursen *et al.*, *Energy Environ. Sci.* **5**, 5577 (2012).
26. A. Han *et al.*, *J. Mater. Chem. A* **3**, 1941 (2015).
27. H. B. Wu *et al.*, *Nat. Commun.* **6**, 1 (2015).